J. Fluid Mech. (1996), *vol.* 313, *pp.* 55–82

Interactions of two jets in a channel: solution multiplicity and linear stability

By RALPH T. GOODWIN AND WILLIAM R. SCHOWALTER

Department of Chemical Engineering, University of Illinois at Urbana–Champaign, Urbana, IL 61801, USA

(Received 24 May 1995 and in revised form 29 September 1995)

The steady, two-dimensional, isothermal flow of an incompressible Newtonian fluid in a semi-infinite channel is modelled using a finite-element method. The flow is driven by injecting two identical jets through symmetrically placed slit-like nozzles into the otherwise closed end of the channel. Multiple steady-state solutions are observed for Reynolds numbers greater than 18.8, where seven solutions have been found. Six of these solutions exist on branches that are not connected to the Stokes flow solution via continuation in the Reynolds number. Further bifurcations of these solutions has led to the discovery of 17 solutions at a Reynolds number of 40. A two-dimensional linear stability analysis of the solution branches shows that for Reynolds numbers in the range of 18.8 to 26.8 there are three stable solutions. One solution is symmetric about the channel centreline while the other two stable solutions are a pair of mirror-image asymmetric flows. For Reynolds numbers in the range 26.8 to 40, there are four known stable solutions consisting of two asymmetric solutions and their mirror-images.

1. Introduction

As one considers the properties of steady solutions to symmetrically formulated boundary-value problems, there are two properties that one might intuitively anticipate. The first is that the solutions will possess the same symmetry as the problem formulation. The second is that there will be a unique symmetric solution. Clearly, both conclusions are true for linear problems. However for nonlinear problems, e.g. Navier–Stokes flows, it is known that neither is necessarily true. Flow through a symmetric sudden expansion in a channel is a well-known example of a flow where the stream function can violate the symmetry of the problem formulation. Fearn, Mullin & Cliffe (1990) present computational results showing that at low flow rates, a steady symmetric flow will occur. However, as the flow rate is increased, an asymmetric flow develops. The asymmetric flow is associated with the presence of a symmetry-breaking bifurcation at a critical flow rate. In this same work, Fearn *et al.* demonstrate experimentally and computationally that instead of a sharp transition from a symmetric flow to an asymmetric one, small imperfections in the flow device cause the transition to be more gradual. At very large flow rates, the flow is observed to become time-dependent.

The infinitely long Taylor–Couette cell flow is a now-classic example of a symmetrically formulated problem having multiple solutions that obey the symmetries of the problem formulation. For low values of the Taylor number, a shear flow is observed. Above the critical Taylor number, roll cells can be observed. As with the

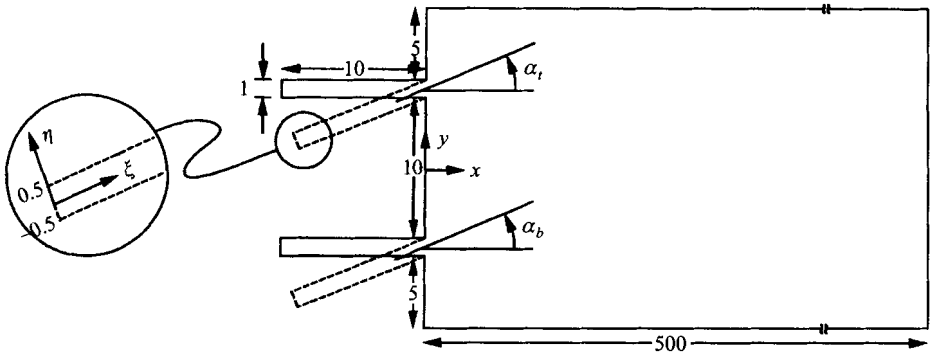

FIGURE 1. Sketch of the computational domain.

problem formulation, both the shear flow and the roll cells were axisymmetric; see for example Benjamin & Mullin (1982).

The present work considers a steady flow that has both several symmetric solutions and a multitude of asymmetric solutions. As in the work of Fearn *et al.* the flow is in a semi-infinite channel. However, instead of a single jet flowing into an expanded channel, the flow here results from the injection into the channel of two jets placed symmetrically between the channel centreline and the channel walls. (See figure 1.)

The motivation for considering this problem stems from work aimed at understanding experiments conducted by Fruman, Perrot & Bouguechal, (1984) who made die swell measurements by injecting a jet of a test fluid into an immiscible density-matched bath. For reference, a jet of a fluid with known rheological properties was injected alongside the jet of test fluid. The problem taken up here is a considerably simplified model of their experiments. That is, all three fluids (that of the bath, the test jet, and the reference jet) are considered to be the same fluid. Furthermore, the model is two-dimensional, whereas the experiment was clearly three-dimensional. Despite these many simplifications, it is hoped that this model will capture the essential nature of the interactions between the test and reference jets.

This problem possesses a large number of solutions for Reynolds numbers greater than 18.8. Thus, to control the scope of this work, attention has been largely restricted to Reynolds numbers in the range 0 to 40.

A detailed description of the problem and numerical methods is presented in §2. The results and conclusions are contained in §§3 and 4.

2. Problem description and numerical methods

This section starts with a description of the problem geometry, equations, and boundary conditions. This is followed by a brief outline of the numerical procedures employed to solve the problem and to study the linear stability of the solutions. The section ends with the definition and discussion of two functionals used to characterize the solutions.

2.1. *Problem description*

Consider the steady two-dimensional isothermal incompressible flow in a semi-infinite channel driven by injecting two identical jets through nozzles in the closed end of the channel. (See figure 1.) A Cartesian coordinate system is established with the abscissa and ordinate coincident with the channel centreline and the closed end of the channel,

respectively. The upper and lower channel walls are located at $y = \pm 11$. The centrelines of the unit-width upper and lower inlet nozzles correspond to the lines $y = \pm 5.5$. The governing equations are

$$Re\,\boldsymbol{u}\cdot\nabla\boldsymbol{u} = \nabla\cdot\boldsymbol{T}, \tag{1}$$

$$\nabla\cdot\boldsymbol{u} = 0, \tag{2}$$

where $\boldsymbol{u} = u\boldsymbol{i}+v\boldsymbol{j}$ is the velocity vector, $\boldsymbol{i}$ and $\boldsymbol{j}$ denote unit vectors in the x- and y-directions respectively, $\boldsymbol{T} = -p\boldsymbol{I}+[\nabla\boldsymbol{u}+(\nabla\boldsymbol{u})^T]$ is the stress tensor, p is the pressure, and $\boldsymbol{I}$ is the identity tensor. The Reynolds number, $Re = Q/2\nu$, is based on the total flow rate in the channel, Q, and the kinematic viscosity of the fluid, ν.

Equations (1) and (2) are solved subject to the following boundary conditions. The no-slip condition is imposed along the nozzle walls, at the closed end of the channel, and along the channel walls,

$$\boldsymbol{u} = \boldsymbol{0} \quad \text{at} \quad \begin{cases} x \geqslant 0, & |y| = 11 \\ x = 0, & 6 \leqslant |y| \leqslant 11 \\ x = 0, & |y| \leqslant 5 \\ x \leqslant 0, & y = \pm 5 \\ x \leqslant 0, & y = \pm 6. \end{cases} \tag{3}$$

The velocity profile at the inflow of each inlet nozzle is parabolic:

$$\boldsymbol{u}\cdot\boldsymbol{n} = -Q_{Nozzle}\,6(1/4-\eta^2), \tag{4}$$

$$\boldsymbol{u}\times\boldsymbol{n} = 0. \tag{5}$$

Here Q_{Nozzle} is the flow rate through the nozzle, $\boldsymbol{n}$ is the outward-pointing unit normal to the computational domain, and η is the ordinate of a local coordinate system with axes coincident with the centreline and inflow plane of each nozzle. (See figure 1). Except in the special circumstances described below, the flow rates through the two nozzles are equal. Consequently, $Q = 2Q_{Nozzle}$ and so $Re = Q_{Nozzle}/\nu$.

To complete the specification of the associated computational problem, the extent of the computational domain is restricted by locating the inflow planes of the inlet nozzles at $x = -10$ and the outflow plane of the channel at $x = 500$. Finally, the normal component of the traction vector is required to vanish at the outflow plane of the computational domain:

$$\boldsymbol{T}:\boldsymbol{n} = 0 \quad \text{at} \quad x = 500. \tag{6}$$

2.2. *Numerical methods*

Equations (1) and (2) are solved numerically using the Galerkin finite-element method. The velocity components are interpolated on each nine-node quadrilateral element using biquadratic basis functions. To achieve element-wise incompressibility, a linear-discontinuous basis is used to interpolate the pressure.

The computational domain is discretized so that the locations of all elements and nodes are symmetric with respect to the channel centreline. Solutions have been computed on six increasingly refined meshes, labelled M1–M6. Table 1 shows the number of elements, nodes and equations associated with each of the meshes. To minimize the computational burden while ensuring accurate solutions, the elements are

Mesh	Elements	Nodes	Equations
M1	700	2961	8022
M2	1572	6527	17770
M3	2800	11521	31442
M4	6300	25681	70262
M5	8582	34891	95528
M6	11216	45509	124666

TABLE 1. Discretization parameters

concentrated near the closed end of the channel and near the channel walls. (See figure 2.) For each mesh, approximately 50% of the elements are concentrated in the region $0 \leqslant x \leqslant 50$.

Except for a high-Re turning point that vanished with grid refinement, the qualitative aspects of the structures of the flows and of the solution-space bifurcation diagram were consistent across all meshes. While there were significant quantitative changes in the locations of bifurcation points when refining from M1 to M2 and from M2 to M3, the bifurcation diagrams for meshes M3 and M4 were nearly coincident. All results presented here were computed on either mesh M3 or M4. Meshes M5 and M6 were used to make a quantitative assessment of the accuracy of solutions computed on meshes M3 and M4. Accordingly, the quantity Ψ_-, to be defined shortly, was computed using meshes M3, M4, M5, and M6 at $Re = 40$ for all solution branches. For any branch, Ψ_- varied by less than 1% between any of meshes M3–M6.

The solution multiplicities reported below are a consequence of the nonlinearity of the momentum equations at non-zero Reynolds numbers. To ensure that the observed nonlinear behaviour was not attributable to a particular numerical treatment of the inertial terms, two different techniques were used to discretize the inertial terms. For most of the computations the inertial terms in (1) were discretized as follows:

$$Re \int_\Omega w\boldsymbol{u}\cdot\nabla\boldsymbol{u}\,\mathrm{d}A, \tag{7}$$

where w is both the weighting function and the velocity basis function, Ω denotes the computational domain, and $\mathrm{d}A$ is a differential area. To gain confidence that the results were not an artifact of the particular numerical procedure used to discretize the nonlinear terms, some of the calculations were repeated using the divergence form of the inertial terms

$$Re(\nabla\cdot\boldsymbol{uu}). \tag{8}$$

Use of the divergence theorem yields the following Galerkin formulation of (8):

$$Re\int_\Omega w\nabla\cdot\boldsymbol{uu}\,\mathrm{d}A = -Re\int_\Omega(\nabla w\cdot\boldsymbol{u})\boldsymbol{u}\,\mathrm{d}A + Re\int_{\partial\Omega} w\boldsymbol{u}\cdot\boldsymbol{nu}\,\mathrm{d}s, \tag{9}$$

where $\partial\Omega$ denotes the computational domain boundary and $\mathrm{d}s$ is a differential arclength. In §3.3 it will be shown that the computations using (9) result in a bifurcation diagram that is essentially identical to those obtained using (7). It is therefore believed that the results presented here are unlikely to be a consequence of errors related either to numerical discretization or to the technique used to discretize the nonlinear terms of the momentum equations.

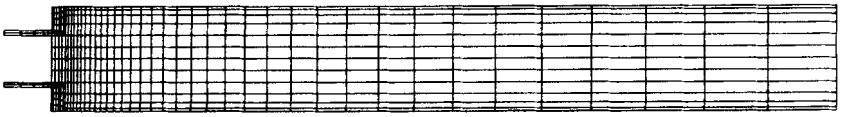

FIGURE 2. The computational mesh M1. Only the portion of the mesh for $x < 150$ is shown. Approximately 50% of the elements are located in the region $x < 50$.

Discretization of (1) and (2) yields a coupled set of nonlinear algebraic equations of the form

$$\boldsymbol{R}(\boldsymbol{X}) = \boldsymbol{0}. \tag{10}$$

Here $\boldsymbol{R}$ is the vector of residual equations and $\boldsymbol{X}$ is the vector of unknowns. These equations were solved iteratively using Newton's method or Newton-like methods. Gaussian elimination via the frontal method (Duff, Erisman & Reid 1989) was used to solve the associated sparse non-symmetric linear system of equations

$$\Delta \boldsymbol{X}^{(k+1)} = -\left[\left(\frac{\partial \boldsymbol{R}}{\partial \boldsymbol{X}}\right)^{(k)}\right]^{-1} \boldsymbol{R}^{(k)}. \tag{11}$$

The convergence criteria were that both $\|\boldsymbol{R}\|$ and $\|\Delta \boldsymbol{X}\|/\|\boldsymbol{X}\|$ be less than 10^{-4}, where $\|\cdot\|$ denotes an L_2 norm.

First-order and arclength parametric continuation schemes (Keller 1977) were used both to reduce the aggregate cost of obtaining solutions and to facilitate solution tracking in the vicinity of bifurcation points.

In any problem where bifurcations are observed, questions of stability arise. Accordingly, the associated two-dimensional linear stability problem has been solved for the leading eigenmodes and eigenvalues. The stability analysis considers two-dimensional disturbances of the form $\boldsymbol{X}(\boldsymbol{x}, t) = \boldsymbol{X}_0(\boldsymbol{x}) + \boldsymbol{X}_1(\boldsymbol{x}, t)$, where $\boldsymbol{x}$ is the spatial position vector, t denotes time, $\boldsymbol{X}_0$ is the steady base-state solution and $\boldsymbol{X}_1(\boldsymbol{x}, t)$ is a time-dependent disturbance quantity. In the usual way, it is assumed that $\boldsymbol{X}_1$ can be represented as $\boldsymbol{X}_1(\boldsymbol{x}, t) = \tilde{\boldsymbol{X}}_1(\boldsymbol{x})\,\mathrm{e}^{\sigma t}$, where the spatial dependence of the eigenfunction, $\tilde{\boldsymbol{X}}_1$, is resolved using finite-element basis functions and the eigenvalue, σ, is possibly complex. This formulation leads to a large sparse generalized non-symmetric eigenvalue problem. Since one is principally interested in the most dangerous eigenmodes, an Arnoldi-based scheme (Sorensen 1992) was used to compute a few of the leading eigenvalues. Since the eigenvalue calculations are rather expensive, the stability calculations could only be performed on meshes M1 and M2. Results are presented for calculations on mesh M2. Because the qualitative features of the flow, as well as the sign-change behaviour of the Jacobian determinant, are consistent across all grids, it is expected that the stability findings are qualitatively correct.

2.3. *Characterizing functionals*

To assist in characterizing solution branches and bifurcation points, it is useful to define a simple scalar measure of the flow. Two measures, Ψ_+ and Ψ_-, are defined as follows. Let $\psi(x, y)$ be the computed stream function, with $\psi(0, 0) = 0$. Let $\psi_p(x, y) = \frac{3}{2}(y/h - \frac{1}{3}(y/h)^3)$ be the stream function for Poiseuille flow in a channel, where h is the channel half-width (here, $h = 11$). Then, with L denoting the computational domain length,

$$\Psi_{\pm} = \int_0^L \int_{-h}^{h} \{[\psi(x, y) - \psi_p(x, y)] \pm [\psi(x, -y) - \psi_p(x, -y)]\}^2 \,\mathrm{d}x\,\mathrm{d}y. \tag{12}$$

The quantities Ψ_+ and Ψ_- have several important properties. First, there will be no contribution to Ψ_+ or Ψ_- from regions where the flow is fully developed. Accordingly, if the computational domain is sufficiently long, then both Ψ_+ and Ψ_- will be independent of the length of the computational domain. Therefore, by evaluating Ψ_+ and Ψ_- for domains of different length, one can determine when the computational domain is sufficiently long. Secondly, $\Psi_\pm$ are measures of a physical property of the flow. Consequently, one should anticipate being able to compute grid-convergent values for $\Psi_\pm$. Third, Ψ_+ is only non-zero for asymmetric flows. Thus, any transition between $\Psi_+ = 0$ and $\Psi_+ > 0$ is a sure indication of a symmetry-breaking bifurcation. Finally, flows that differ only by reflection about the centreline of the channel, i.e. mirror-image flows, are mapped to the same values of Ψ_+ and Ψ_-.

3. Results

As will be shown, the problem considered here possesses several solutions for all values of the Reynolds number greater than 18.8. Each solution can be categorized by whether or not it is accessible via continuation in the Reynolds number starting with the Stokes flow solution. The branches of solutions accessible by continuation in Re starting with the $Re = 0$ solution are described first. This is followed by a discussion of a novel geometric continuation procedure used to access solutions not connected to the Stokes flow solution. Next, the bifurcation structure of each solution branch is explored as the Reynolds number is varied. It is then shown that a second form of geometric continuation will separate all known solution branches into two families of branches. It will be argued that this second form of geometric continuation systematically reveals all members of each of the two families of branches. As a consequence, several new branches of solutions are uncovered.

Throughout this section, the topology of the stream function will be illustrated by plotting the critical points (minima, maxima, and saddle points) of the stream function and the streamlines associated with critical points, separation points, and reattachment points. So that the reader can compare the various solution branches, plots of stream functions with critical points are shown for each branch at $Re = \{0, 10, 20, 25, 30, 40\}$, if the branch exists at that Reynolds number.

3.1. *Solutions connected to the Stokes flow solution*

Starting from the symmetric stable and unique Stokes flow solution, a set of solutions is obtained by first-order continuation in Re. This set of solutions is called branch I. Figure 3 shows stream-function critical points plots for solutions on branch I with Reynolds numbers in the range 0 to 40. As noted earlier, the stream function datum is set to 0 at the midpoint of the closed end of the channel, i.e. $\psi(0, 0) = 0$. Accordingly, $\psi(x \geqslant 0, y = \pm 11) = \pm 1$.

Clearly, branch I is a set of symmetric solutions. At the lowest Reynolds numbers, the dominant feature in the stream-function topology is the presence of the recirculation regions in the corners of the channel. As the Reynolds number is increased, a pair of centreline-bordering recirculation regions develops. The strength of these centreline-boarding recirculation regions, as measured, for example, by the difference between the values of the stream function at the dividing streamline and the recirculation centre, increases with Re. For high enough Re, the flow in these regions is essentially inviscid. At $Re \approx 24.5$ another pair of recirculation regions develops along the upper and lower channel walls approximately one channel-width downstream of the closed end of the channel. If the Reynolds number is sufficiently high, the location

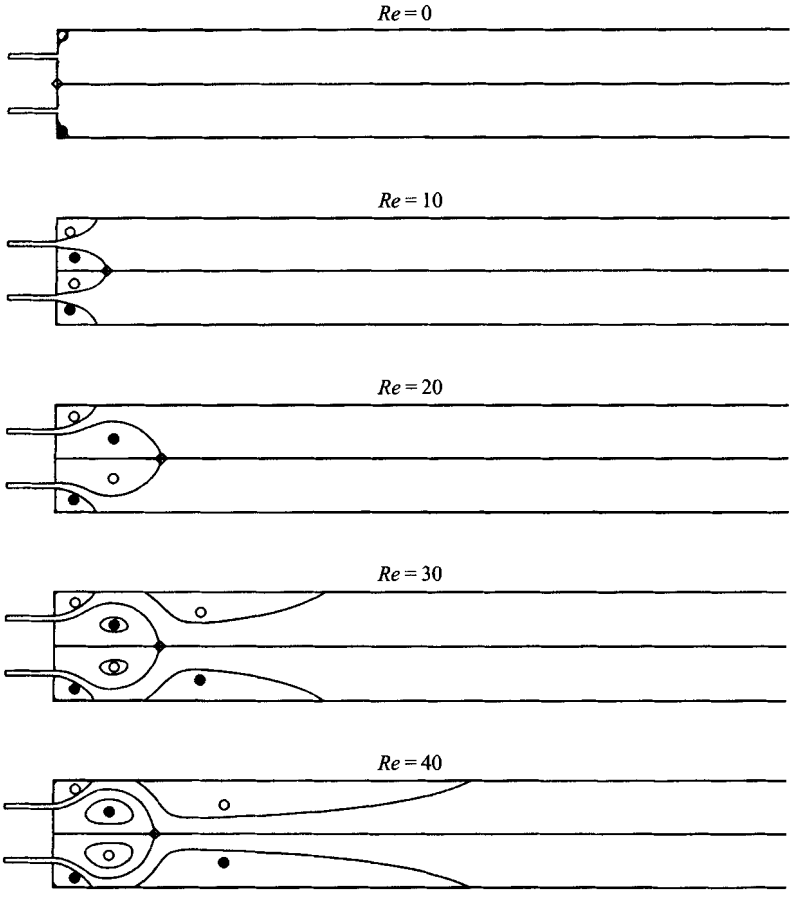

FIGURE 3. Stream-function critical points and contours on branch I. In this and subsequent similar figures, minima are denoted by filled circles, maxima by open circles, and saddle points by diamonds.

of the downstream reattachment point of these downstream recirculation regions is observed to grow approximately linearly with increases in Re.

3.1.1. *Asymmetric solutions*

As Re was increased along Branch I, it was noted that the determinant of the Jacobian matrix of the discretized nonlinear equations changed sign in the interval $26 < Re < 28$, and again in the interval $38 < Re < 40$. This change in the sign of the Jacobian determinant, together with the continued success of first-order continuation, signalled that two bifurcation points had been encountered, neither of which were turning points. This suggested that the bifurcations may be symmetry-breaking bifurcations.

To access the alleged asymmetric solutions, the following physically motivated procedure was used. Starting with a symmetric solution at a Reynolds number just above the value corresponding to the approximately located bifurcation point, the flow rates in the two inlet nozzles were made unequal. This was done in a fashion that preserved the total channel flow rate, and thus the channel Reynolds number. With the flow rates in the two nozzles unequal, the Reynolds number was increased to 40 using first-order continuation. At $Re = 40$, the inlet-nozzle flow rates were rebalanced, thus restoring a symmetric problem formulation, and an asymmetric flow was observed.

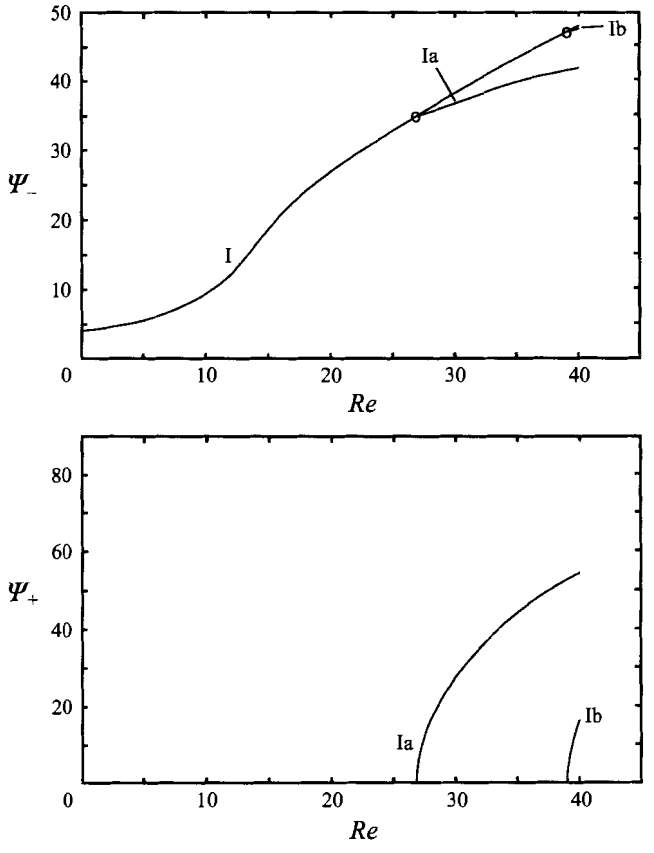

FIGURE 4. Bifurcation diagram showing the solution branches connected to the Stokes flow solution by continuation in Re, branches I, Ia, and Ib. Since branch I is symmetric, $\Psi_+ = 0$. Thus, there is no curve for branch I in the bottom plot. Bifurcation points are circled.

Starting with the asymmetric $Re = 40$ solutions, each asymmetric branch was tracked back to the bifurcation point on branch I by lowering Re, again using first-order continuation.

An alternative, more mathematically motivated, procedure for accessing the asymmetric branches would be to add a multiple of the null vector of the Jacobian matrix to the symmetric solution at the bifurcation point. The mathematical foundation for this type of procedure can be found in the work of Werner & Spence (1984).

These two asymmetric branches are labelled Ia and Ib in figure 4. The bifurcation of branch Ia from branch I is evident in figure 4, where a new branch is seen to fork off the branch I curve in the plot of Ψ_- versus Re, at $Re = 26.85$. In the plot of Ψ_+ versus Re, a curve is seen to emanate from the abscissa at the same Reynolds number, indicating that the flow is asymmetric. The features in figure 4 associated with the bifurcation of branch Ib are similar, with the bifurcation occurring instead at $Re = 39.0$. (Note, the solutions computed on branches Ia and Ib each represent one of a pair of asymmetric mirror-image flows. The mirror-image of these flows can be obtained by repeating the above-described procedure while reversing the choice of which of the two inlet nozzles has the greater flow rate.)

The stream-function critical point plots for the solutions on branch Ia at $Re = 30$ and 40 and on branch Ib at $Re = 40$ are shown in figure 5. Notice that the topology

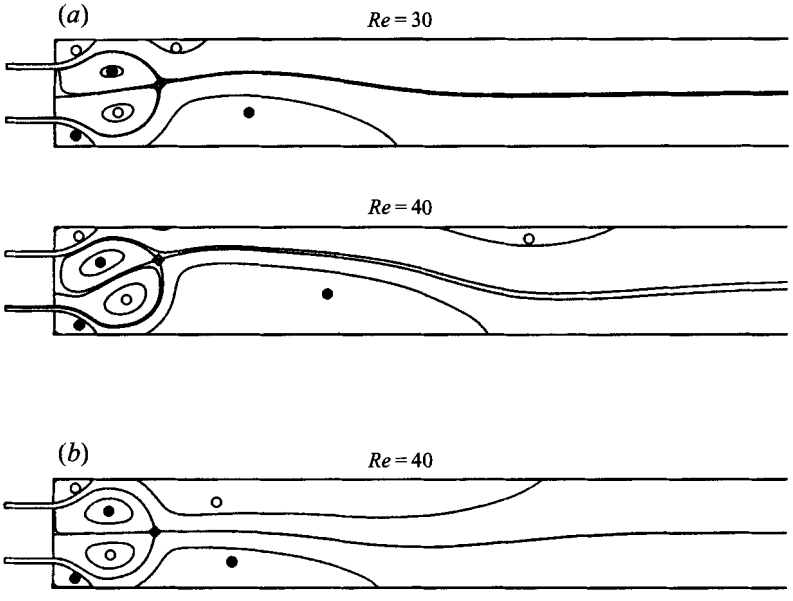

FIGURE 5. Stream-function critical point plots for branches Ia(*a*) and Ib(*b*).

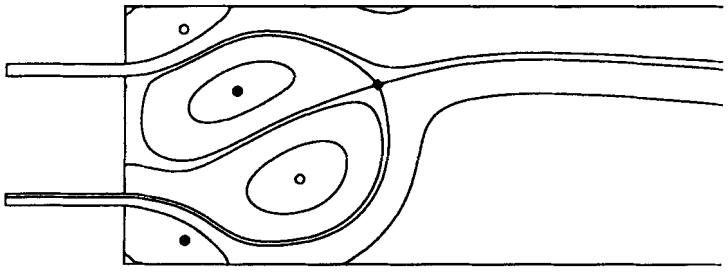

FIGURE 6. Detailed view of the streamline that divides the flow issuing from the lower nozzle for the branch Ia $Re = 40$ solution. Since at the saddle point $\psi = -0.211$, roughly 21 % of the fluid leaving the lower nozzle travels a serpentine path towards the saddle point, then back towards the rear channel wall before finally heading downstream.

of branch Ia is clearly different from that of branch I. In particular, compare the streamlines connected to the saddle point near the middle of the channel at $Re = 40$. On branch I this streamline, a contour of $\psi = 0$, terminates at the lower corner of the upper nozzle, the upper corner of the lower nozzle and at the midpoint of the closed end of the channel. In short, it separates the centreline-bordering recirculation regions from the flow exciting the nozzles. The situation for branch Ia, shown in detail in figure 6, is completely different. At $Re = 40$ the streamline associated with the saddle point is a contour of $\psi = -0.211$. As a consequence, the streamline enters the bottom nozzle, dividing the flow from the nozzle into two streams. The lower stream follows a path much like the path followed by fluid leaving the lower nozzle in the branch I solution. The upper stream follows a more tortuous path. The fluid exits the nozzle and moves downstream towards the saddle point. Then, it reserves direction and heads towards the rear channel wall. At the channel wall the stream flows vertically upwards to the upper nozzle before finally heading downstream, once again flowing past the saddle point. This feature of the stream-function topology is not merely a curiosity nor is it a plotting error. As indicated by the value of the stream function, the flow rate in this

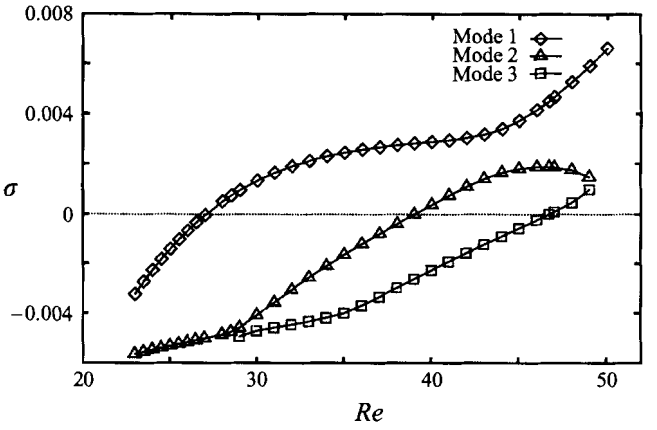

FIGURE 7. The most dangerous eigenvalues for branch I. The eigenvalues are purely real in the range shown. Modes 2 and 3 coalesce to form a complex-conjugate pair near $Re = 49$. Mode 3 becomes purely real near $Re = 29$ owing to the coalescence of a complex-conjugate pair of eigenvalues.

stream constitutes more than 20% of the total flow leaving the lower nozzle at $Re = 40$. Furthermore, it will be shown that it is branch Ia and not branch I that is the stable flow for $Re > 26.85$.

While most of this work focuses on flows for $Re \leqslant 40$, exploratory (but grid-refined) calculations were made for Re up to 105. These calculations revealed additional symmetry-breaking bifurcations of branch I in the ranges $46 \leqslant Re \leqslant 47$, $60 \leqslant Re \leqslant 61$, $80 \leqslant Re \leqslant 81$, and $104 \leqslant Re \leqslant 105$. Thus, the pattern of repeated bifurcations of branch I appears to persist as the Reynolds number is increased. However, there is no apparent regularity in the spacing of the bifurcation points.

3.1.2. *Linear stability analysis*

The associated two-dimensional linear stability problem has been solved for the most dangerous eigenmodes. Branch I is stable for $Re < 26.85$. In the range $26.85 \leqslant Re \leqslant 40$, branch Ia is stable, whereas branch I is unstable to a purely real eigenmode. At the bifurcation point of branch Ib, branch I becomes unstable to a second subdominant purely real eigenmode. Branch Ib is unstable to a real eigenmode.

Figure 7 shows the most dangerous eigenvalues of branch I as a function of the Reynolds number. In the range $30 \leqslant Re \leqslant 49$, the fastest growing modes are purely real. As expected, one eigenmode becomes unstable at the Reynolds numbers corresponding to each of the first three symmetry-breaking bifurcations of branch I. Note that the eigenmode associated with the bifurcation of branch Ia remains the most dangerous eigenmode, over the explored range of Re. The slowest growing of the three modes, labelled mode 3 in figure 7, results from the coalescence of a complex-conjugate pair just below $Re = 30$. Similarly, near $Re = 49$, the eigenvalues of the two subdominant modes, modes 2 and 3, coalesce to form a complex-conjugate pair of eigenvalues. Figure 8 shows contours of the two components of velocity for each of the two fastest-growing eigenmodes, modes 1 and 2, near the Reynolds number where each eigenmode becomes unstable. Consistent with the requirements for a symmetry-breaking bifurcation, each eigenmode is antisymmetric with respect to reflection about the channel centreline. That is to say, the symmetry of each velocity component is opposite to that found in the base-state flow. Thus, u of the eigenmode is an odd function of y, while v of the eigenmode is an even function of y.

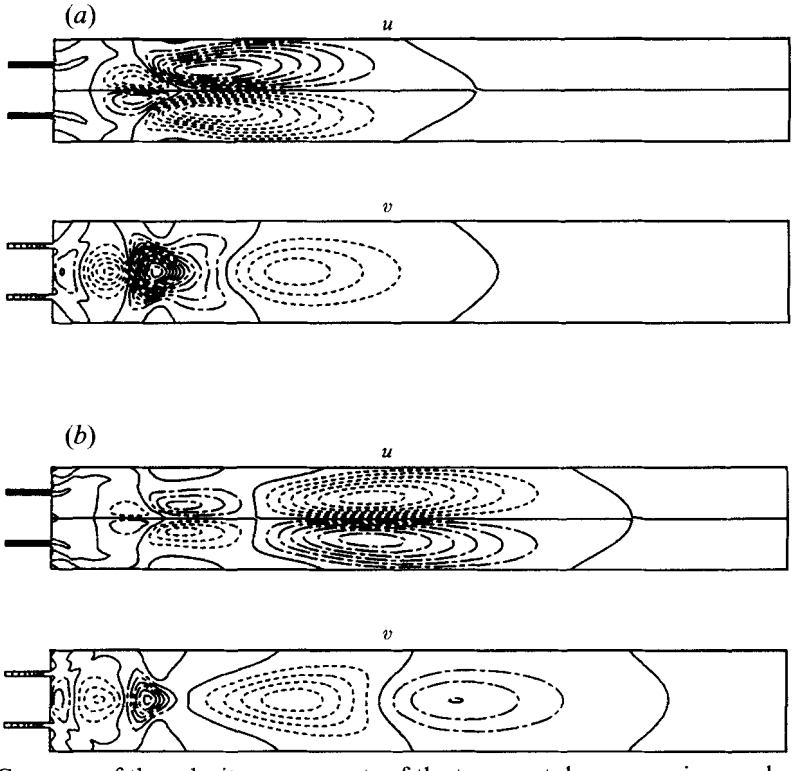

FIGURE 8. Contours of the velocity components of the two most dangerous eigenmodes of branch I near the Reynolds number where the mode becomes unstable. The zero contour is denoted by a solid line, positive ——, and negative by — — —. The contours of u are spaced at intervals of 0.005, while v contours are separated by 0.0025. (*a*) Mode 1, $Re = 27$; (*b*) mode 2, $Re = 39$.

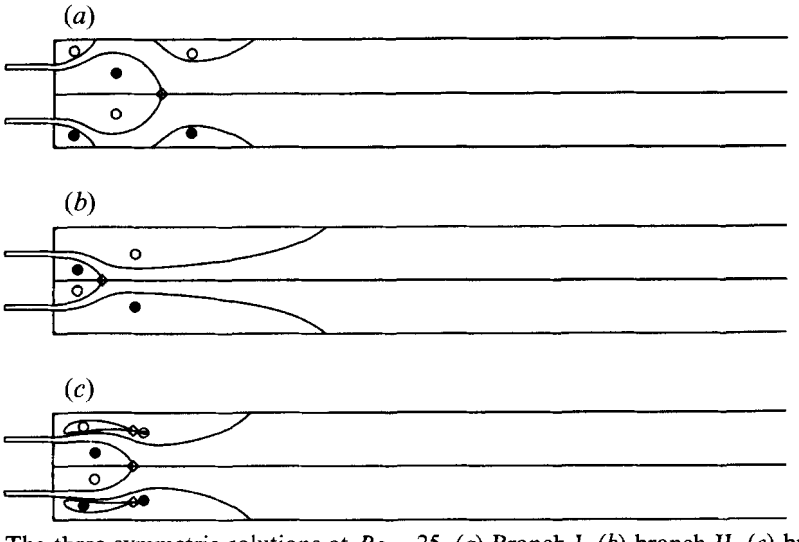

FIGURE 9. The three symmetric solutions at $Re = 25$. (*a*) Branch I, (*b*) branch II, (*c*) branch III.

Finally, consideration of figures 3 and 4 together demonstrates that qualitative changes in the stream-function topology do not result in simultaneous changes in the stability of the flow nor in the occurrence of bifurcations. For example, branch I becomes unstable at $Re = 26.85$ without a qualitative change in the stream-function topology. On the other hand, the development of new recirculation regions along the upper and lower walls near $Re = 24.5$ does not coincide with a change in stability. This is not to say that qualitative changes in the stream-function topology do not ultimately play some role in changing the stability characteristics of the flow.

3.2. *The existence of other branches*

In the early stages of this study, preliminary calculations were made in which the flow was assumed to be symmetric with respect to the channel centreline. As a consequence, the computational domain consisted of only the lower half of the channel. In those calculations, the inflow nozzles were also absent. Instead, the jets were assumed to enter the channel with a perfectly parabolic velocity profile. Again, starting with the Stokes flow solution, branch I was tracked via first-order continuation in the Reynolds number. Unlike the full problem, no bifurcations were detected until $Re \approx 325$, where a turning point was encountered, and the Reynolds number could be increased no further. Using arclength continuation, the turning point was rounded to a new symmetric branch, branch II. This branch was tracked down to a Reynolds number near 19, where another turning point was discovered. Rounding this turning point led to as third symmetric solution branch, branch III. The Reynolds number was increased along this third branch to beyond $Re = 400$ without finding any additional turning points.

The three symmetric solutions at $Re = 25$ (computed on the full problem domain with inlet nozzles) are shown in figure 9. In contrast to solutions on branch I, where the flow exiting the nozzles turns towards the nearest channel wall, solutions on branches II and III are characterized by fluid turning towards the channel centreline as it exits the nozzles. In addition, the combination of corner vortices and downstream wall-attached recirculation regions seen on branch I are replaced by a pair of large recirculation regions. Each of these recirculation regions occupies all of the channel between the nozzle and the nearest channel wall, and extends downstream to roughly the same location as the reattachment point of branch I downstream vortices. Notice that on branch III, these recirculation regions contain a figure-eight streamline. As evidenced by the unequal size of the two lobes of the figure-eight, the saddle point and second extrenum form at a cusp-like point on a streamline surrounding the initial extremum, as opposed to, for example, the initial extremum splitting into two extrema and a saddle point. This appears to be the standard mechanism for critical point generation inside of recirculation regions.

In consideration of the work of Acrivos & Schrader (1982), where the effects of varying inflow conditions for high-Re flow into a planar symmetric expansion were examined, it was decided to recompute the symmetric solutions to the present problem using a computational domain that had an inflow nozzle. The purpose of the nozzle was to provide a length over which the velocity profile could relax from parabolic to some more realistic condition before entering the channel.

Figure 10 shows the deviation of each component of velocity from a parabolic profile at $x = 0$ for the lower nozzle of the full problem at $Re = 40$ on branch I. The components of the dimensionless deviation velocity are defined as $\Delta u = u_{computed} - 6(1/4 - \eta^2)$ and $\Delta v = v_{computed}$. Note that both Δu and Δv are non-zero. Moreover, Δv is negative over the lower 80% of the nozzle width, indicating that most

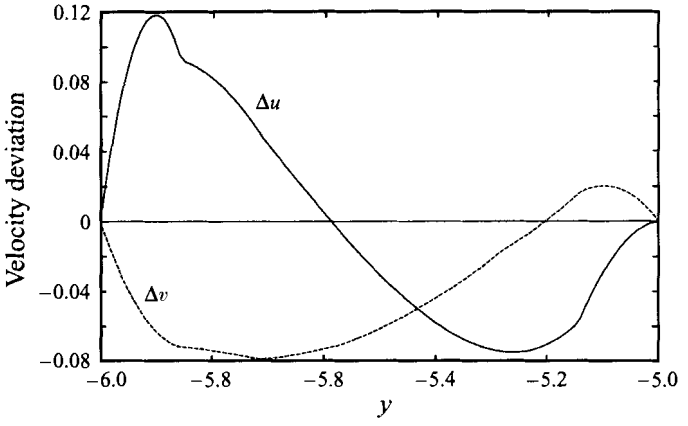

FIGURE 10. Deviation of each component of velocity from a fully developed parabolic profile at the exit of the lower inlet nozzle on branch I at $Re = 40$. The discontinuities in the slopes of the velocity profiles occur at element boundaries and are therefore a reflection of the discretization.

of the flow is turning towards the lower channel wall. This is clearly contrary to the purely horizontal entrance flow obtained by specifying a parabolic velocity profile. (The discontinuties in the slopes of the velocity components are a manifestation of the discretization.) The deviation from a parabolic velocity profile is a consequence of strong centreline-bordering recirculation near the closed end of the channel. The strength of this recirculating region, and therefore presumably the magnitude of the deviation of the inlet velocity profile, increases as the Reynolds number is increased. It is therefore perhaps not surprising that the turning point on branch I at $Re \approx 325$ was no longer present when an inlet nozzle was added to the computational domain of the symmetric problem. As a result, it was impossible to access the other two symmetric solution branches via continuation in Reynolds number. Still, there was evidence of the existence of two other symmetric branches. Consequently, alternative continuation schemes were sought.

3.3. *Symmetric nozzle angle variation*

The other symmetric solution branches were found to be accessible by changing the angle of the inflow nozzles. The motivation for this tactic stems from the observation that the fluid turns towards the channel wall as it enters the channel for flows on branch I, whereas on branch II the fluid turns towards the channel centreline as it enters the channel. Hence, it was hoped that if $Re > 19$, a region of Re where three symmetric solutions were believed to exist, one might be able to selectively access the three symmetric solution branches by aiming the inflow nozzles either towards the centreline or towards the channel walls.

For convenience, the continuation technique is described in terms of the full problem. Referring to figure 1, let α_t and α_b be the counterclockwise angles, measured in degrees, between the axis of the top or bottom nozzle and the channel centreline. The axis of a nozzle is defined to be the line between the midpoint of the inflow plane of the nozzle and the midpoint of the associated channel inflow slit. Note that except when the nozzles are horizontal, there is a narrowing of the width of the nozzle between the nozzle inflow plane and the channel inflow slit. For each nozzle, this is a geometric consequence of requiring the channel inflow slit to have unit width while also requiring the nozzle inflow plane to be of unit width and perpendicular to the nozzle axis. The width of the nozzle at the channel inflow slit is given approximately by the cosine of

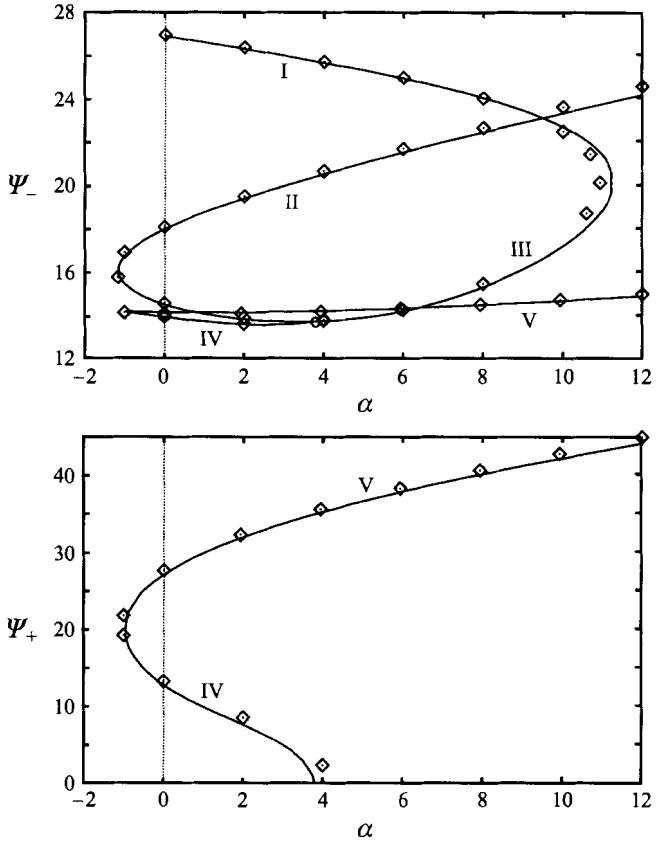

FIGURE 11. Bifurcation diagram for symmetric nozzle angle variation at $Re = 20$. Bifurcation points are distinguished from coincidental branch crossings by the presence of a circle. The results of discretizing the inertial terms using (7) are shown using a solid line while the diamonds are the results from when (9) was used.

the nozzle inclination angle. To maintain the geometric symmetry, the nozzle angles are restricted such that $-\alpha_t = \alpha_b$. For notational convenience, the subscript of α is dropped, letting $\alpha = \alpha_b$. Finally, the description of the location of the nozzle walls in the specification of the no-slip condition (3) is modified appropriately.

Returning to the full-domain problem, solutions on branch I have been computed and now solutions are sought on symmetric branches II and III. Following the strategy learned in the preliminary work on the half-channel problem, α was first increased starting with the branch I $Re = 20$ solution. Increasing α amounts to pointing the nozzles towards the channel centreline. Consequently, the flow out of the nozzles is directed towards the channel centreline, consistent with the stream-function topology on branches II and III. Figure 11 is the bifurcation diagram resulting from this geometric continuation procedure. As expected, by directing the nozzles toward the channel centreline, a turning point, i.e. a different solution branch, is encountered at $\alpha = 11.2°$. Rounding this turning point leads to symmetric solution branch III. As α is lowered back towards zero, the Jacobian determinant was observed to change sign at about $\alpha = 3.96°$, once again signalling the presence of a branch of asymmetric solutions. Further decreases in α led to a second turning point at $\alpha = -1.15°$, and thus to the third symmetric branch of solutions, branch II. Using symmetry-breaking

techniques similar to those described above, the asymmetric solutions associated with the Jacobian determinant changing sign were mapped out. These branches are labelled IV and V. Branch IV results from a symmetry-breaking bifurcation of branch III at $\alpha = 3.96°$. Branches IV and V are connected by a turning point at $\alpha = -0.95°$.

As part of the effort to ensure that the observed solution multiplicities were not due to the method of discretizing the inertial terms, the computations described in the preceding paragraph were repeated using the divergence form of the inertial terms, (9). The diamonds in figure 11 are the results obtained using (9) while the solid lines are the results of using (7). Mesh M4 was used in both computations. Since the bifurcation diagram is substantially independent of whether the inertial terms were discretized using (7) or (9), the solution multiplicites are unlikely to be a numerical anomaly.

Some comments can be made about the stability of these solutions based on the structure of the bifurcation diagram and the symmetry of the solution branches. First, recall that when doing *Re* continuation along branch I, the first bifurcation occurs at $Re = 26.85$. Thus, since the Stokes flow solution is stable, so is the $Re = 20$ branch I solution. Branch III must be unstable because the turning point between symmetric branches I and III is associated with an odd number of eigenvalues crossing the imaginary axis. Assume that the odd number is one. (This can be confirmed with the stability analysis.) Since both branches I and III are symmetric, the null vector of the Jacobian at the turning point must also be symmetric. Therefore, the unstable eigenmode of branch III is is symmetric with respect to the channel centreline. The symmetry-breaking bifurcation between branches III and IV is also associated with an eigenvalue crossing into the unstable half-plane. Since branch IV is asymmetric, the unstable eigenmode must be antisymmetric. Accordingly, one deduces that branch IV is unstable and that branch III is unstable to two eigenmodes, one symmetric, the other antisymmetric, for α between the symmetry-breaking bifurcation point of branch IV and the turning point between branches II and III. As branches II and III are both symmetric, one can conclude that an eigenvalue affiliated with a symmetric mode has crossed the imaginary axis. However, without doing the stability calculations, one cannot ascertain whether this mode is the unstable mode of branch III passing back into the stable half-plane, or if branch II is unstable to two symmetric modes. Nevertheless, it is clear that branch II is unstable to the same antisymmetric mode as branch III. So far as the stability of branch V is concerned, no information may be gained from the bifurcation diagram. Like the transition between branches II and III, the turning point between branches IV and V may be due to the stabilizing of the unstable mode of branch IV, or due to a new eigenmode becoming unstable. Only the stability analysis will resolve this issue.

By using Leray–Schauder degree theory, Benjamin (1978) has shown that at almost any parameter value there must be an odd number of solutions, k, and that at least $(k-1)/2$ of these solutions must be unstable. We will call this Result I. Satisfying Result I does not prove that all of the solution branches have been found. On the other hand, failure to satisfy Result I is proof that there are undiscovered solution branches. At this point seven solutions have been found at $(Re, \alpha) = (20, 0°)$. Branches I, II and III are symmetric. Branches IV and V are associated with asymmetric solutions and therefore represent two solutions each. Only branch I is currently known to be stable. For every value of α, figure 11 is consistent with the requirements of Result I.

Starting with the $(Re, \alpha) = (20, 0°)$ solutions, the Reynolds number dependence of each solution branch is now considered. Figure 12 plots $\Psi_{\pm}$ as a function of the Reynolds number for each of branches I–V. The curves for branches I, Ia, and Ib are the same as in figure 4. Branch II undergoes a symmetry-breaking bifurcation at

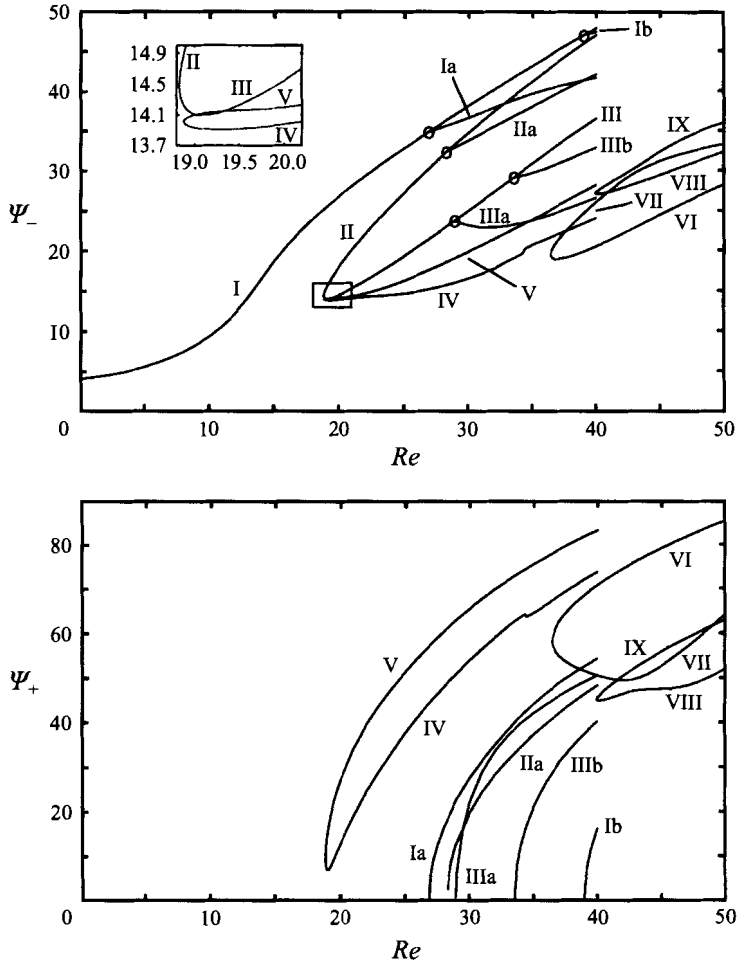

FIGURE 12. The bifurcation structure as Re is varied. A magnified view of the boxed region of the top panel is shown as an inset. Note that branch II connects to branch III via a turning point. Similarly, a turning point connects branches IV and V.

$Re = 28.3$. This new asymmetric branch is labelled IIa. Similarly, branch III has a symmetry-breaking bifurcation at $Re = 29.0$ and again at $Re = 33.5$. These new branches are labelled IIIa and IIIb, respectively. The kink that appears on branch IV near $Re = 35$ shows up as a sigmoidal segment with two closely spaced ($Re = 34.81$ and 35.25) turning points when mesh M3 is used and as a kink when meshes M2 and M4 (shown) are used. As shown in the inset of the top panel of figure 12, as the Reynolds number is reduced below 20 one finds that branches II and III are connected by a turning point at $Re = 18.83$. Likewise, branch IV connects to branch V via a turning point at nearly the same value of the Reynolds number, $Re = 18.88$. As a consequence of these two turning points, branch I appears to be the unique set of solutions when the nozzles are horizontal and $Re < 18.8$. Finally, we note that the symmetry-breaking bifurcation points associated with branches Ia, Ib, IIa, IIIa, and IIIb were all verified by repeating these computations using the divergence form of the inertial terms, thus reinforcing the belief that the observed nonlinearities were not solely a consequence of the specific manner in which the inertial terms were discretized.

Stream-function critical point plots for branches II, IIa, III, IIIa, IIIb, IV, and V at a selection Reynolds numbers are shown in figure 13. Of interest is the common occurrence of saddle points in the stream-function topology. In fact, on branch IIIb at $Re = 40$, a figure-eight streamline is seen inside one lobe of another figure-eight streamline. Also note that the mid-channel saddle point is clearly associated with $\psi \neq 0$ on branches IIIa and IV. Thus, as on branch Ia, the flow from one of the nozzles on both of these branches is divided into two streams that follow very different paths.

It is important to recognize that solution branches II and III, as well as IV and V, appear to be unconnected to the branch I solutions if one's view is limited to their Reynolds-number-based connectivity. However, continuation in the nozzle angle makes clear that all known solution branches can be connected by continuation in a single parameter. This suggests that one might learn more about the structure of the solution space by performing this type of continuation at other Reynolds numbers. Accordingly, this geometric continuation procedure was repeated starting with solutions $Re = 18.75$ and 31.

Since the structure of the bifurcation diagrams is expected usually to have a continuous parametric dependence, one anticipates that the $Re = 18.75$ bifurcation diagram will look largely like the diagram at $Re = 20$, except that the turning points between branches II and III, and between branches IV and V will occur at a positive value of α. Thus, the line $\alpha = 0°$ will not cross any of these four branches. Figure 14 shows that this easily anticipated morphogenesis of the bifurcation diagrams is in fact correct. A magnified view of the boxed region of figure 14 is shown in the inset of the top panel, where it can be seen that the general structure of the bifurcation of branch IV from branch III is similar to that shown at $Re = 20$ in figure 11, except that branch IV exists only in the small range $0.12° \leqslant \alpha \leqslant 0.21°$.

At $Re = 31$, the solution-space structure is known to be richer, since all three symmetric branches have had exactly one symmetry-breaking bifurcation by this Reynolds number. The associated bifurcation diagrams are shown in figure 15. Careful comparison of figure 12 at $Re = 31$ with figure 15 at $\alpha = 0°$, shows that the two figures are completely consistent. The branches resulting from Reynolds-number-continuation symmetry-breaking bifurcations of branches I, II, and III are all accounted for in figure 15 at $\alpha = 0°$. In addition, one observes, for example, that branch IIIa is connected to branch III by two symmetry-breaking bifurcations. Thus if one starts with the $\alpha = 0°$ branch IIIa solution and then either increases or decreases α sufficiently, the branch IIIa solution will degenerate to the branch III solution. Also note the loop in branch III near $\alpha = 8°$. Recall that branch III is symmetric. The loop indicates the presence of two additional symmetric branches (five in total) at this nozzle angle. In the next section, it will be argued that undiscovered symmetric branches must occur in pairs, as has happened on branch III.

We note that it is not unheard of to discover solution branches that are not connected to the principal solution branches by 'natural' or obvious continuation parameters. In the context of the Taylor problem, Anson, Mullin & Cliffe (1989) have investigated so-called anomalous modes that are not connected to the Couette flow solution.

There are several stability-related questions that still need settling. The number of unstable eigenmodes as well as the dominant instability of branch II are not resolved. It is not clear which of the two unstable branch III eigenmodes is most dangerous. Finally, the stability of branches IIa, IIIa, IIIb, and V is unknown. Attention will be restricted to the stability of solutions at $\alpha = 0°$. Consider first branches IIIa and IIIb. Both branches result from symmetry-breaking bifurcations of branch III. Like the

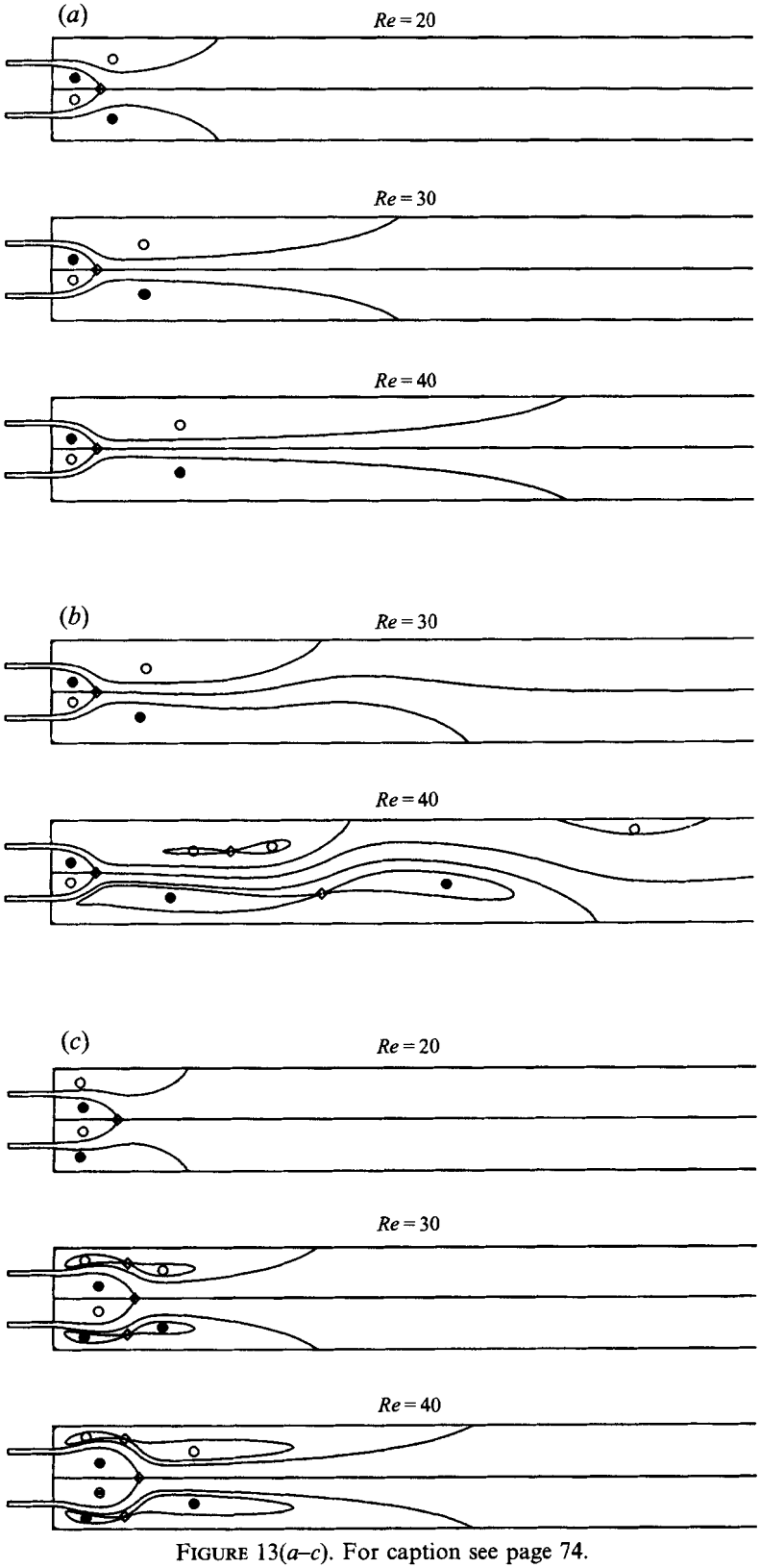

FIGURE 13(*a–c*). For caption see page 74.

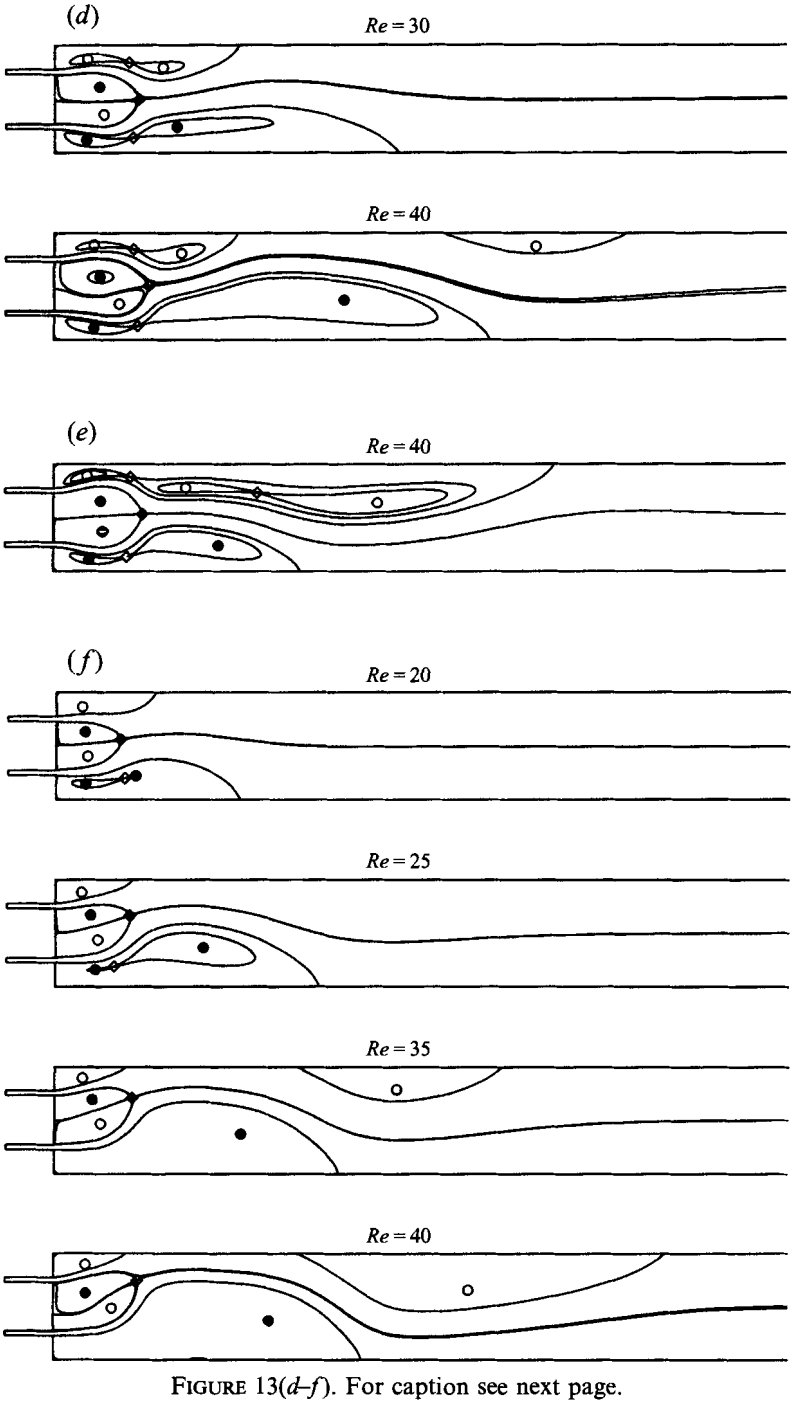

FIGURE 13(*d–f*). For caption see next page.

symmetry-breaking bifurcations of branches Ia and Ib from branch I, these bifurcations involve the eigenvalue of an antisymmetric eigenmode crossing the imaginary axis. The stability of symmetric eigenmodes is unaffected by the bifurcations. Accordingly, since branch III has an unstable symmetric eigenmode, then branches IIIa and IIIb must

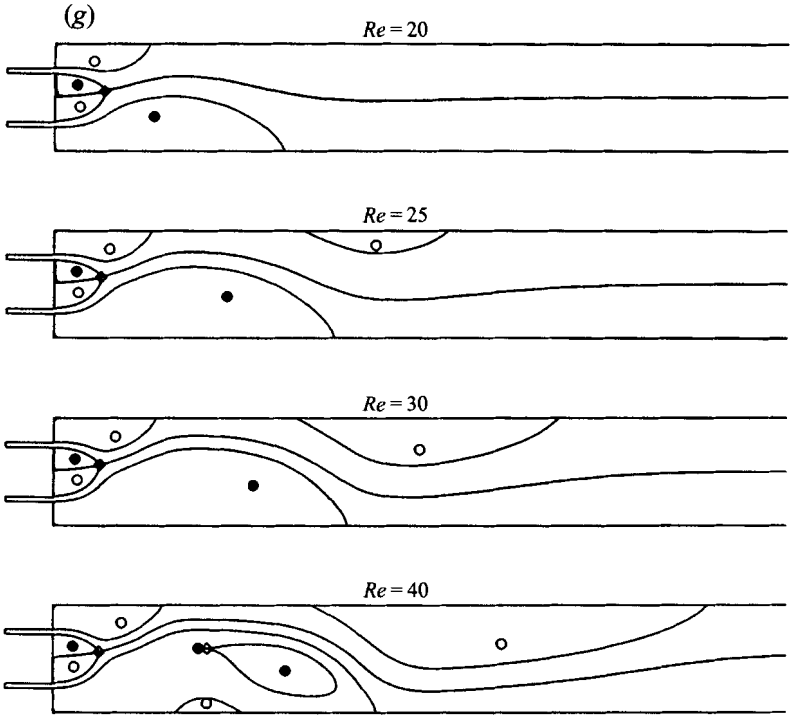

FIGURE 13. Stream functional critical point plots for branches II(*a*), IIa(*b*), III(*c*), IIIa(*d*), IIIb(*e*), IV(*f*), and V(*g*).

also be unstable (though the unstable eigenmode has no special symmetry properties). Figure 16 shows the most dangerous eigenvalues as a function of the Reynolds number for branches II and III. The most dangerous eigenmodes for branch III are purely real for $Re \leqslant 40$. In the range $33.5 \lesssim Re \leqslant 40$, the most dangerous eigenmode is antisymmetric. Below $Re \approx 33.5$ until the turning point to branch II, the most dangerous eigenmode of branch III is symmetric. At the turning point between branches II and III, the eigenvalue associated with the symmetric eigenmode passes into the stable half-plane. Thus, as shown in figure 16, branch II is unstable to the same antisymmetric mode as branch III. Since branch II is unstable to an antisymmetric mode, the stability of branch IIa cannot be determined from symmetry considerations. The stability analysis shows that the eigenvalue associated with a second real antisymmetric eigenmode crosses into the unstable half-plane when branch IIa bifurcates from branch II. Therefore branch IIa is unstable. Figure 17 shows the Reynolds-number dependence of the eigenvalues for the two fastest growing modes of branch IV near the turning point to branch V. Both eigenmodes are purely real. One mode is unstable, the other decays. At the turning point between branches IV and V, these two real modes combine to form a pair of stable oscillatory modes. Thus, branch V is shown to be a stable branch. There are therefore three stable solutions in the range $18.83 < Re < 26.85$, the branch I solution and the pair of mirror-image solutions of branch V. In the range $26.85 < Re < 40$, there are four stable solutions, the branch Ia solutions and the branch V solutions. Note that the solutions on both branch Ia and branch V are asymmetric.

Finally, many of the results of this section can be obtained by other forms of symmetry-preserving geometric continuation. For example, the transitions between the

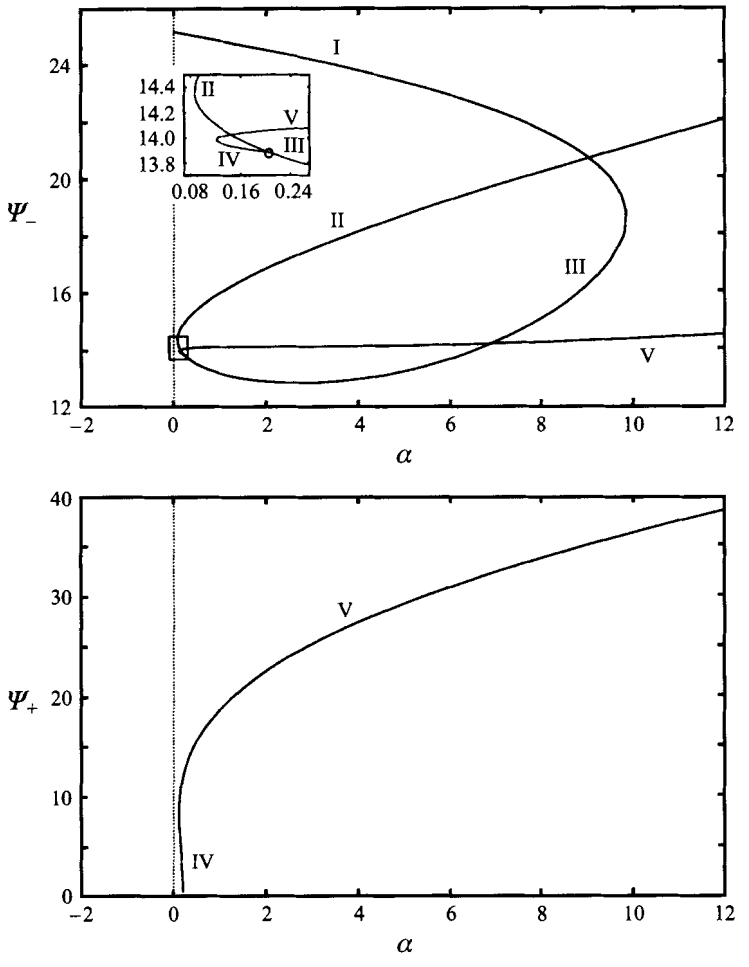

FIGURE 14. Bifurcation diagram for symmetric nozzle angle variation at $Re = 18.75$. An enlarged view of the boxed region of the top panel is presented as an inset. Note that the turning points between branches II and III and between branches IV and V occurs at $\alpha > 0°$ and that therefore these branches do not exist when the inlet nozzles are horizontal.

symmetric branches, I, II and III at $Re = 20$ have been effected by varying the width of the channel while preserving the positions of the nozzles with respect to the channel centreline. The physical motivation for this procedure was to attempt to modulate the strength of the interactions between the two jets compared to the strength of the interaction of either jet with the nearest channel wall. It seems likely however that results concerning a variable-width channel are less amenable to experimental verification than are results for a channel with tilting inlet nozzles.

3.4. *Parallel nozzle angle variation*

Recall that the bifurcation diagram, figure 12, satisfies Result I at each value of the Reynolds number. Counting mirror-image flows individually, this gives a total of 17 known solutions at $Re = 40$. Of these, only the two pairs of asymmetric solutions associated with branches Ia and V are linearly stable to two-dimensional disturbances. While satisfaction of Result I is gratifying, it should be emphasized that this does not prove that all of the steady solutions to this problem have been found.

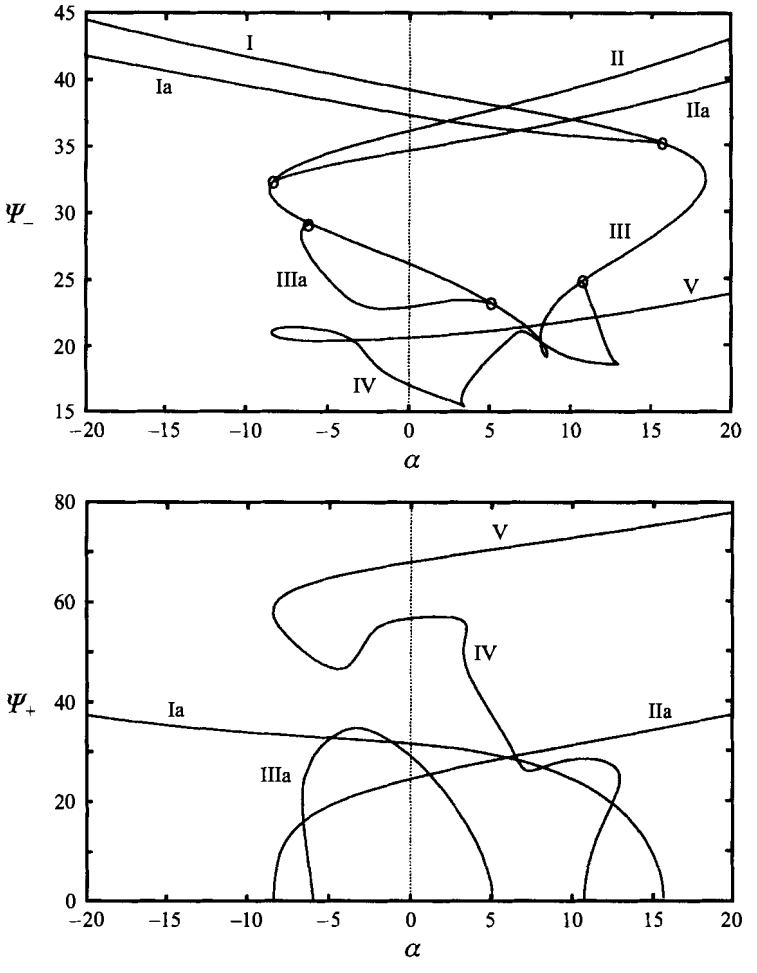

FIGURE 15. Bifurcation diagram for symmetric nozzle angle variation at $Re = 31$.

It is however possible to demonstrate that all of the known solutions can be divided into a small number of families (two). More importantly, the process of dividing the known solutions into families will systematically find every as-yet-unidentified member of each family of solutions. (To avoid confusion, these families are not the families of solutions connected or not connected to the Stokes flow solution, referred to earlier.)

To identify the families of solutions, a variant of the procedure for changing solution branches by changing the angle of the inflow nozzles is used. Previously, the nozzles were moved in a fashion that maintained the symmetry of the problem specification. That restriction is now altered, instead requiring that $\alpha_t = \alpha_b$. Thus, the nozzles are moved in a way that causes their axes to remain parallel. The symmetry of the problem formulation is broken whenever $\alpha \neq 0°$. Attention is focused on the $\alpha = 0°$ solutions that are encountered using this style of geometric continuation. (As before, the subscripts on α are omitted.)

Consider the form of a continuation diagram of α versus $\Psi_\pm$. Suppose one starts with a symmetric solution, say the branch I $Re = 20$ solution, and then increases α. This will result in an asymmetric flow. If, instead, α had been decreased by the same

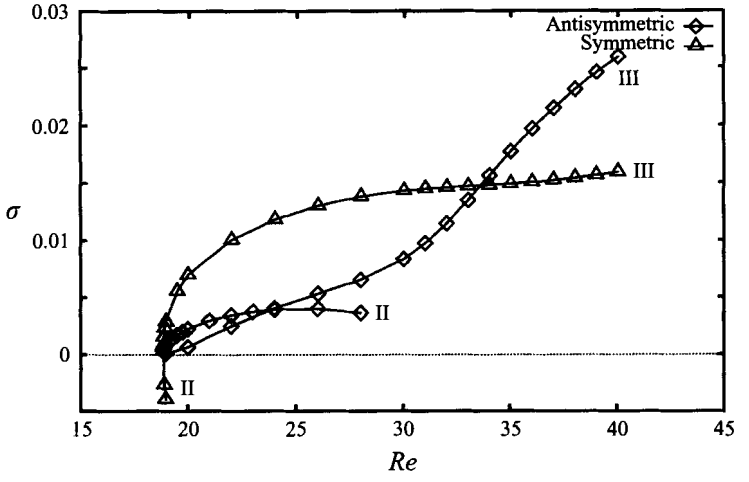

FIGURE 16. Most dangerous eigenvalues for branches II and III. At the turning point from branch III to branch II, the eigenvalue associated with the symmetric eigenmode passes into the stable half-plane, while the eigenvalue associated with asymmetric eigenmode remains unstable.

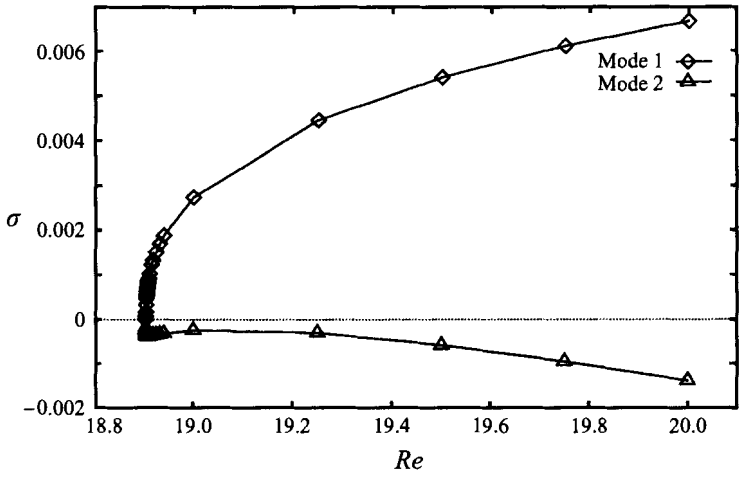

FIGURE 17. The two most dangerous eigenvalues for branch IV. At the turning point from branch IV to branch V, the two real eigenvalues combine to form a stable complex-conjugate pair.

amount, one would find the mirror-image flow, since the starting solution is symmetric. Clearly, the continuation diagram is symmetric about the line $\alpha = 0°$.

The procedure is therefore to start with a symmetric solution at a fixed Reynolds number and then to increase α. At some point, either a turning point will be encountered and therefore α must be decreased, or the physical limit of $\alpha = 90°$ will be reached. (In practice the limit of $\alpha = 90°$ is never reached since the elements discretizing the nozzle become excessively distorted at very large nozzle angles. Continuation was typically terminated at $\alpha \approx 80°$.) If $\alpha = 90°$ is reached, then the starting solution is the only member of this family of solutions. (To be clear, the members of the family are restricted to only those solutions, symmetric or asymmetric, that exist when the nozzles are horizontal, i.e. when $\alpha = 0°$. Thus, while there is a continuum of solutions as α is varied, attention is confined to solutions to the symmetric, $\alpha = 0°$, problem.) If a

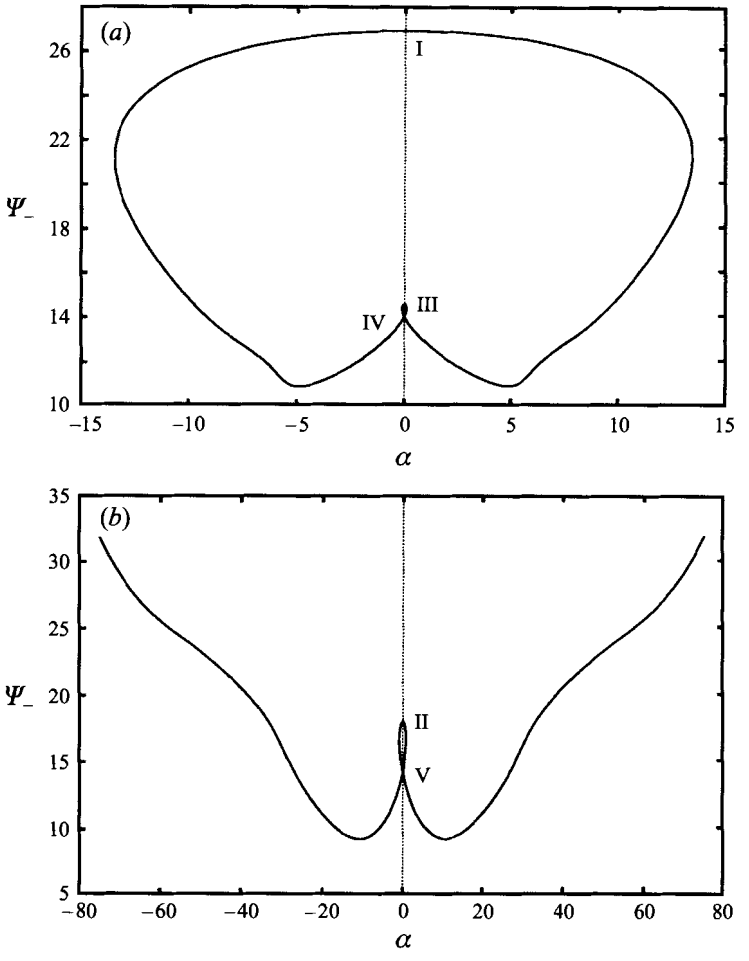

FIGURE 18. Bifurcation diagram for parallel nozzle angle variation at $Re = 20$.

turning point is encountered, then one is at the start of a potentially long continuation path that has perhaps many turning points, and that could pass many times through $\alpha = 0°$. There are only two eventualities for this continuation path. The first is that α reaches $\pm 90°$ and thus, as before, all of the solutions have been found. The complete set of solutions to the symmetric problem (for this family) is found by cataloguing all of the crossings of the line $\alpha = 0°$. Except for the crossing due to the initial symmetric solution, each crossing of the line $\alpha = 0°$ represents one of a pair of mirror-image asymmetric solutions. Thus, the total number of solutions in this family is odd. The other, more interesting, possibility is that the solution trajectory returns to a different symmetric solution at $\alpha = 0°$. In this case, the mirror-image path will be traced back to the starting symmetric solution. Thus, a closed loop is formed. Again, the places where the solution trajectory crosses $\alpha = 0°$ comprise the members of this family of solutions to the symmetric problem. In this case, the total number of solutions in the family is even. Note that while a continuous path may cross the line $\alpha = 0°$ many times, at least one, and at most two, of those crossings correspond to symmetric solutions. Furthermore, if a closed-loop family of solutions is found, then to satisfy Result I, a family of solutions must exist that terminates at $\alpha = \pm 90°$.

Careful consideration of the implications of using this form of continuation, along

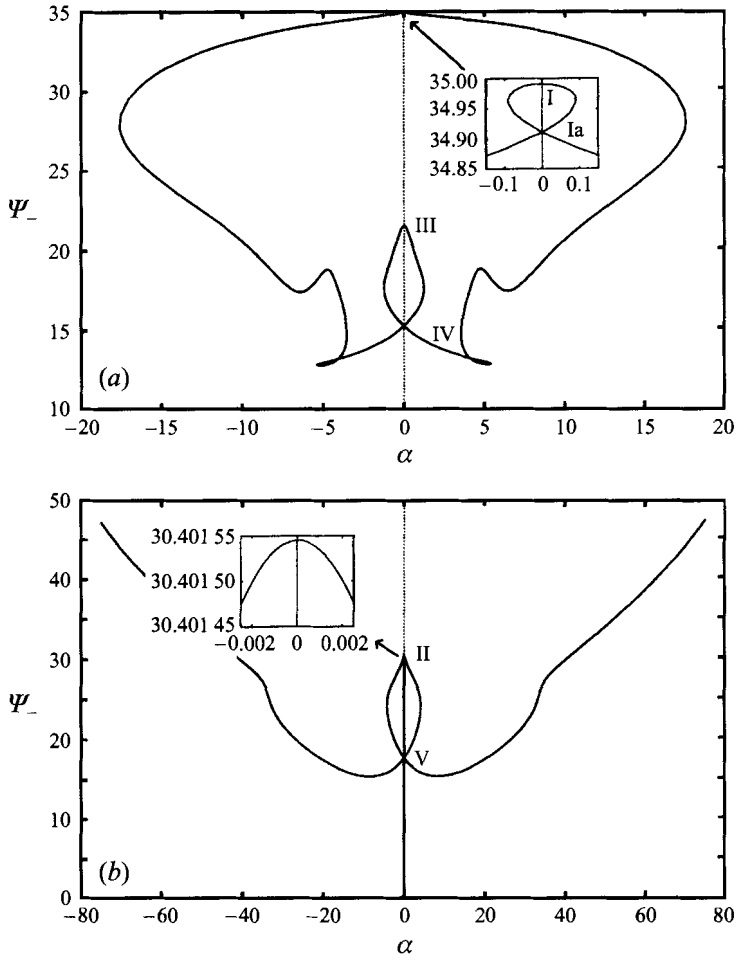

FIGURE 19. Bifurcation diagram for parallel for parallel nozzle angle variation at $Re = 27$. The inset of (*a*) shows that both branches I and Ia are found near $\Psi_- = 35$. The inset of (*b*) shows that the $\alpha = 0°$ crossing associated with branch II does so with zero slope, as would be expected for a symmetric branch.

with the requirement that the total number of solution branches is odd, allows one to draw conclusions about the number and symmetry of any undiscovered solutions. First, note that if a new branch of solutions is found, then it must belong to a new family of solution branches, since, as has been shown, the continuation procedure systematically reveals all members of the known families. Next, observe that all solution families are either of the closed-loop variety, with an even number of family members, or of the open-ended variety (called this because the continuation path terminates at $\alpha = \pm 90°$) with an odd number of family members. Suppose the newly discovered branch is symmetric. If it is a member of an open-ended family, then once all of the members of this new family have been found, the total number of members of all families will be even, and this is forbidden. Therefore, there must be another open-ended family of solutions. Moreover, this family must contain one member that is a symmetric solution. Suppose instead that the new symmetric solution belonged to a closed-loop family. In this case, the new family has a second symmetric member.

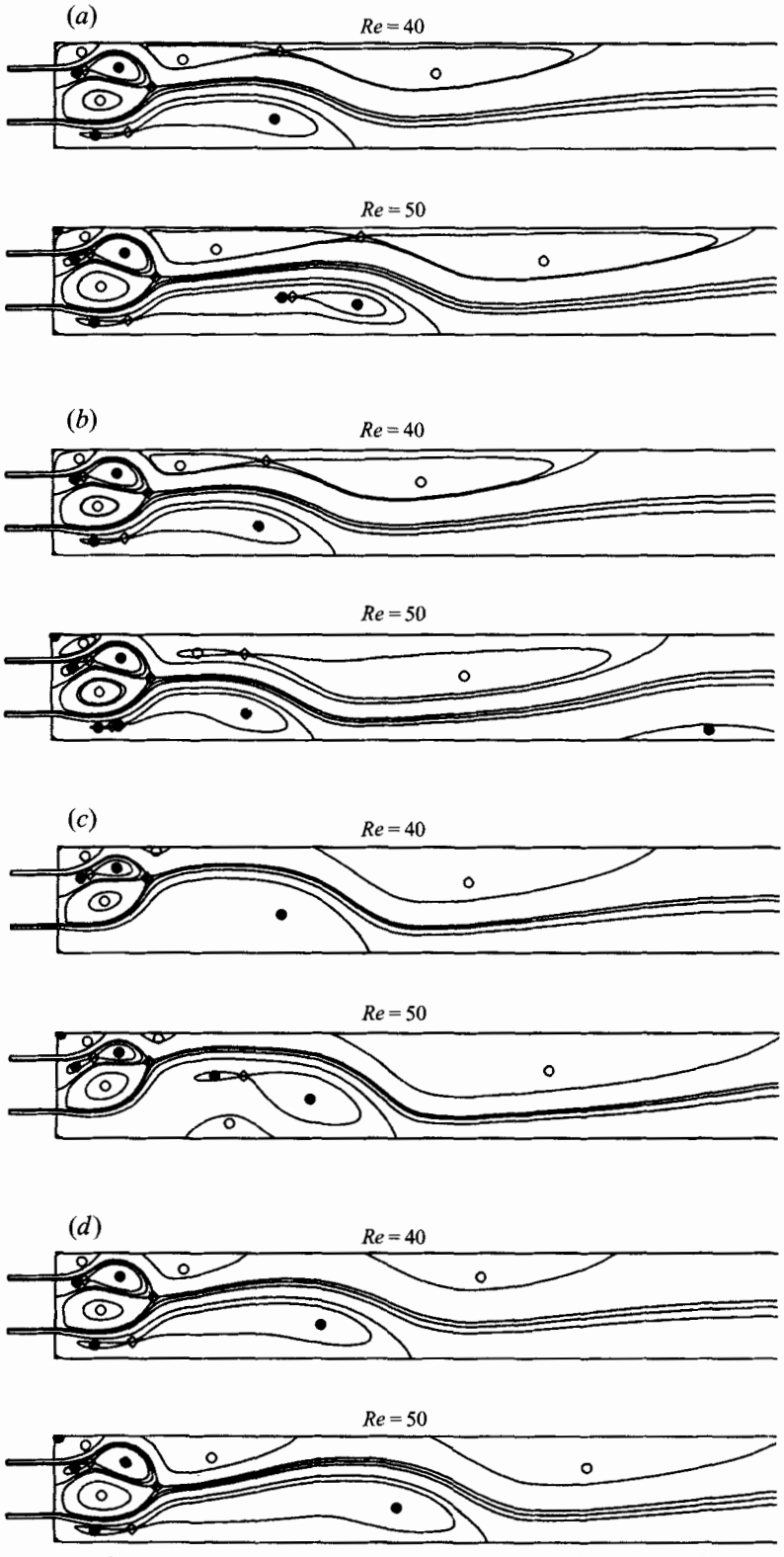

FIGURE 20. Stream-function critical point plots for branches VI(*a*), VII(*b*), VIII(*c*), and IX(*d*).

Also, since closed-loop families have an even number of members, the requirement that the total number of solutions be odd is satisfied. Thus, if the newly found solution is symmetric, then there must be another missing symmetric solution. A similar line of reasoning applied to newly discovered asymmetric solutions leads to the conclusion that for this case also, one must find a new pair of symmetric solutions. In short, if there are any as-yet-undiscovered solutions, then at least two of them are symmetric solutions. Moreover, the total number of missing symmetric solutions must be even. Obviously, since asymmetric solutions occur in mirror-image pairs, the total number of missing asymmetric branches must also be even.

This continuation procedure has been used at $Re = 20$, 27 and 40. At each Reynolds number, the solution branches segregate into two families. One family is of the closed-loop type and contains symmetric branches I and III. The other family is open-ended and is associated with symmetric branch II.

Figure 18 shows the continuation diagrams at $Re = 20$. Since the problem formulation, and therefore the solutions, cannot be symmetric if $\alpha \neq 0°$, only Ψ_- is shown. Figure 18(*a*) shows the closed-loop family. This family of solutions crosses the $\alpha = 0°$ line four times. There is one crossing for each of branches I and III and one crossing for each of the branch IV solutions. Similarly, in figure 18(*b*), there is a total of three $\alpha = 0°$ crossings; once for branch II and once for each mirror-image of branch V. Note that the total number of crossings, seven, is consistent with the earlier findings about the number of solutions at $Re = 20$ with the nozzles horizontal.

The continuation diagram for $Re = 27$ is shown in figure 19. At this Reynolds number, only branch I has undergone a symmetry-breaking bifurcation. The aim is to determine if branch Ia is associated with either of the two known families, or with a new family. The inset in figure 19(*a*), a close-up view of figure 19(*a*) in the vicinity of $\Psi_- = 35$, $\alpha = 0°$, shows that branch Ia is a member of the closed-loop family of solutions. Once again, the total number of crossings in the closed-loop and open-ended families of solutions demonstrates that all previously known solution branches have been accounted for, and no new solution branches have been found.

When this procedure was repeated at $Re = 40$, there were eight more crossings in the closed-loop family than could be accounted for based on the known solution branches. These new crossings are due to four previously unseen asymmetric branches. The new branches are labelled VI–IX. As before, the open-ended family has crossings due to branches II and V. In addition, there is a pair of crossings associated with branch IIa. The Reynolds number dependence of all solution branches is shown in figure 12. Branches VI and VII connect via a Reynolds number turning point at $Re = 36.5$. Similarly, branches VIII and IX connect by a turning point at $Re = 39.9$. (The fictitious turning point mentioned earlier connects branches VII and IX, and vanishes if the mesh is sufficiently fine.) Like branches II, III, IV and V, branches VI–IX are not connected to the Stokes flow solution via continuation in Re. It would not be surprising to learn that branches VI–IX connect with the other solution branches via symmetric nozzle angle continuation. However, this has not been verified. Stream-function critical point plots of branches VI–IX at $Re = 40$ and 50 are shown in figure 20. In the light of the facts that the eigenvalue calculations are excessively expensive for meshes finer than M2 and that reliable solutions for branches VI–IX could not be obtained on grids M1 or M2, the stability calculations have not been made for these solution branches.

4. Summary

A computational study of the base-state and two-dimensional linear stability of the flow in a semi-infinite channel driven by the side-by-side injection from two jet-like nozzles into the otherwise closed end of the channel has been presented. The problem formulation is symmetric with respect to the channel centreline. Multiple symmetry-breaking bifurcations of the branch of solutions connected to the Stokes flow solution occur as the Reynolds number is increased with the nozzle axes parallel with the channel axis. The preliminary calculations beyond $Re = 40$ suggest that the symmetric branches will continue to undergo symmetry breaking as the Reynolds number is increased. It was also shown that by manipulating the angles of the nozzles, one could access several branches of solutions not connected to the Stokes flow solution. Of particular interest is the fact that the number of these disconnected branches also seems to increase as the Reynolds number is raised. Of note is that one of these solution branches, branch V, is a stable branch. It is not obvious from this work how one might access branch V experimentally since all numerical avenues traverse unstable branches.

The full implications of these calculations for an experimentalist are unclear. There are, however, indications that the observed flow may be extremely sensitive to small variations in the channel geometry or in the way an experiment is conducted. For example, when the nozzles were moved symmetrically at $Re = 20$, the turning points between branches II and III and between branches IV and V were close to $\alpha = 0°$. (See figure 11.) This suggests that seemingly minor misadjustments of the nozzles may inadvertently cause experimentally determined bifurcation diagrams to vary significantly from those shown here.

We gratefully acknowledge the computational support provided by the National Center for Supercomputing Applications and by the IBM Corporation through the Shared University Research program.

REFERENCES

ACRIVOS, A. & SCHRADER, M. L. 1982 Steady flow in a sudden expansion at high Reynolds numbers. *Phys. Fluids* **25**, 923–930.

ANSON, D. K., MULLIN, T. & CLIFFE, K. A. 1989 A numerical and experimental investigation of a new solution to the Taylor vortex problem. *J. Fluid Mech.* **207**, 475–487.

BENJAMIN, T. B. 1978 Bifurcation phenomena in steady flows of a viscous fluid. *Proc. R. Soc. Lond.* A **359**, 1–26.

BENJAMIN, T. B. & MULLIN, T. 1982 Notes on the multiplicity of flows in the Taylor experiment. *J. Fluid Mech.* **121**, 219–230.

DUFF, I. S., ERISMAN, A. M. & REID, J. K. 1989 *Direct Methods for Sparse Matrices.* Oxford University Press.

FEARN, R. M., MULLIN, T. & CLIFFE, K. A. 1990 Nonlinear flow phenomena in a symmetric sudden expansion. *J. Fluid Mech.* **211**, 595–608.

FRUMAN, D. H., PERROT, P. & BOUGUECHAL, J. 1984 On the swelling of submerged jets of dilute and semi-dilute polymer solutions. *Chem. Engng Commun.* **27**, 101–118.

KELLER, H. B. 1977 Numerical solution of bifurcation and nonlinear eigenvalue problems. In *Applications of Bifurcation Theory* (ed. P. H. Rabinowitz), pp. 359–384. Academic.

SORENSEN, D. C. 1992 Implicit application of polynomial filters in a k-step Arnoldi method. *SIAM J. Matr. Anal. Apps.* **13**, 357–385.

WERNER, B. & SPENCE, A. 1984 The computation of symmetry-breaking bifurcation points. *SIAM J. Numer. Anal.* **21**, 388–399.